Draft of June 3, 2019
Preprint typeset using LaTeX style emulateapj v. 12/16/11

# SN 2018 FIF: A LARGE RED SUPERGIANT EXPLOSION DISCOVERED IN ITS INFANCY BY THE ZWICKY TRANSIENT FACILITY

Authors + Builders

*Draft of June 3, 2019*


## ABSTRACT

High cadence transient surveys are able to capture supernovae closer and closer to their first light. Applying analytical models to such early emission, we can constrain the progenitor stars properties. In this paper, we present observations of SN 2018 fif (ZTF18abokyfk). The supernova was discovered close to first light and monitored by the Zwicky Transient Facility (ZTF) and the *Swift* space telescope. Early spectroscopic observations suggest that the progenitor of SN 2018 fif was surrounded by relatively small amounts of circumstellar material compared to a handful of previous cases. This specificity, as well as the high cadence multiple-band coverage, makes it a good candidate to investigate using shock cooling models. We employ the `SOPRANO` code, an implementation of the model by Sapir & Waxman (2017) that has the advantage of being self consistent by including a careful account for the model validity time domain. We find that the progenitor of SN 2018 fif was a large red super-giant, with a radius of $R = 1204^{+121.52}_{-176.31}\,R_{\odot}$ and an ejected mass of $M_{\rm ej} = 10.5^{+6.4}_{-0.0}\,M_{\odot}$. Our model also gives information on the explosion epoch, the progenitor inner structure, the shock velocity and the extinction. The large radius differs from previously modeled objects, and the difference could be either intrinsic or due to the relativeley small amount of CSM around SN 2018 fif, perhaps making it a "cleaner" candidate for applying shock cooling analytical models.


## 1. INTRODUCTION

In recent years, advances in the field of high-cadence transient surveys have made it possible to systematically discover and follow-up Supernovae (SNe) within hours of their first light (e.g., Nugent et al. 2011; Gal-Yam et al. 2014; Yaron et al. 2017; Arcavi et al. 2017; Tartaglia et al. 2017). This offers several new opportunities to understand the early stages of core collapse (CC) SN explosions and to identify the nature of their progenitor stars.

First, rapid spectroscopic follow-up in the hours following first light has led to the detection of "flash ionized" emission from infant SNe (Gal-Yam et al. 2014; Khazov et al. 2016; Yaron et al. 2017; Hosseinzadeh et al. 2018). These events show transient prominent high-ionization recombination emission lines in their spectra, a signature of confined circumstellar material (CSM) ionized by the SN shock-breakout flash ("flash spectroscopy"). Khazov et al. (2016) has shown that $\sim 20\%$ of the SNe discovered by the Palomar transient factory (PTF) within 10 days of explosion are "flashers", while recent results from ZTF (Bruch et al, in preparation) suggest that the fraction of such events may be even higher for events observed earlier, and that confined CSM around CC SNe progenitors is common.

Second, the observational access to the first hours following the explosion has offered a new opportunity to test theoretical models of early emission from CC SNe and constrain their progenitor properties. The handful of cases where direct pre-explosion observations of progenitors exist (e.g., Smartt 2015, and references therein) suggest that many type II SNe arise from red supergiants, a population of stars with radii ranging from about $100\,\mathrm{R}_{\odot}$ to $1500\,\mathrm{R}_{\odot}$ (e.g., Levesque 2017, and references therein). In recent years, theorists have developed analytical models linking SN early multi-color light curves to progenitor properties, such as its radius, mass, or inner structure. Recent papers by Morozova et al. (2016) and Rubin & Gal-Yam (2017) review and compare these models. In this paper, we use the recent model by Sapir & Waxman (2017) (SW17), which has two advantages. First, it accounts for bound-free absorption in the calculation of the color temperature, a specificity that may have a large impact on the estimation of the progenitor radius. Second, it extends the previous results by Rabinak & Waxman (2011) to later times, making additional observations useful in this analysis.

Comparison between early observations of CC SNe and theoretical predictions were performed in the past (e.g. by Gall et al. 2015; González-Gaitán et al. 2015; Rubin & Gal-Yam 2017; Hosseinzadeh et al. 2019). Rubin & Gal-Yam (2017) account for the limited temporal validity domain of these models - which some of the other analysis do not - but were limited to r-band observations. To our knowledge, SN 2013 fs (Yaron et al. 2017) is the only published object for which high cadence multiple-band observations are available and which was modeled with the SW17 model, using a methodology accounting for the time validity of this model. However, the spectroscopic observations of SN 2013 fs - the best observed "flasher" to date - show evidence for $\sim 10^{-3}\,M_{\odot}$ of confined CSM surrounding the progenitor. The presence of CSM casts doubt upon the validity of the SW17 model in this case, and perhaps could have pushed the best-fit model radius found for this object ($R = 100 - 350 R\odot$) towards the lower end of the RSG radius distribution. A "cleaner" supernova, with no prominent signatures of CSM around the progenitor, may be a more appropriate test-case for the SW17 model.

In this paper, we present and analyse the UV and visible-light observations of SN 2018 fif (ZTF18abokyfk), a SN first detected shortly after explosion by the Zwicky Transient Facility (ZTF; e.g., Bellm et al. 2019; Graham

TABLE 1

| Parameter | Value |
|---|---|
| right ascension $\alpha$ ($J2000$) | 2.360644 deg |
| declination $\delta$ ($J2000$) | 47.354093 deg |
| redshift $z$ | $z = 0.017189$ |
| distance modulus $\mu$ | 34.31 mag |
| galactic extinction $E_{B-V}$ | 0.10 mag |

NOTE. — Basic parameters of SN 2018 fif.

et al. 2019) as part of the ZTF extragalactic high-cadence experiment (Gal-Yam 2019).

We present the aforementioned observations of SN 2018 fif in §2. In §3, we present the analysis of these observations, and the spectroscopic evidence making SN 2018 fif a good candidate for modeling. §4 is dedicated to the modeling of the shock cooling phase of SN 2018 fif and the derivation of the progenitor parameters. We then summarize our main results in §5.

## 2. OBSERVATIONS AND DATA REDUCTION

In this section, we present the observations of SN 2018 fif by ZTF and *Swift*.

### 2.1. *Discovery*

SN 2018 fif was first detected on 2018 August 21 at 8:46 UT by the ZTF (Bellm et al. 2019; Graham et al. 2019) wide-field camera mounted on the 1.2 m Samuel Oschin telescope (P48) at Palomar Observatory. ZTF images were processed and calibrated by the ZTF pipeline (Masci et al. 2019). A duty astronomer reviewing the ZTF alert stream (Patterson et al. 2019) via the ZTF Growth Marshal (Kasliwal et al. 2019) issued an internal alert, triggering follow-up with multiple telescopes, using the methodology of (Gal-Yam et al. 2011). This event was reported by Fremling (2018) and designated SN 2018fif by the IAU Transient Server (TNS[1]). The SN is associated with the $B = 14.5$ mag galaxy UGC 85 (Falco et al. 1999), shown in Figure 1. The coordinates of the object, measured in the ZTF images are $\alpha = 00^h09^m26^s.55$, $\delta = +47^d21'14''.7$ (J2000.0). The redshift $z = 0.017189$ and the distance modulus $\mu = 34.31$ mag were obtained from the NASA/IPAC Extragalactic Database (NED) and the extinction was deduced from Schlafly & Finkbeiner (2011) and using the extinction curves of Cardelli et al. (1989). These parameters are summarized in Table 1.

Previous ZTF observations were obtained in the months prior to the SN explosion and the most recent non-detection was on 2018 August 20 at 11:30, i.e. less than 24 hours before the first detection. We present a derivation of the explosion epoch in § 3.1.

### 2.2. *Photometry*

SN 2018 fif was photometrically followed in multiple bands for $\sim 5$ months. Light curves are shown in Figure 2. The photometry is reported in electronic Table 2 and is available from the Weizmann Interactive Supernova data REPository[2] (WISeREP, Yaron & Gal-Yam 2012).

[1] https://wis-tns.weizmann.ac.il/
[2] https://wiserep.weizmann.ac.il

TABLE 2

| Epoch (jd) | Mag (magAB) | Flux ($10^{-17}$erg/s/cm$^2$/Å) | Instrument |
|---|---|---|---|
| 2458351.866 | $19.11 \pm 0.06$ | $5.756 \pm 0.318$ | P48/R |
| 2458351.937 | $18.78 \pm 0.10$ | $15.10 \pm 1.391$ | P48/G |
| 2458353.697 | $18.18 \pm 0.02$ | $15.263 \pm 0.281$ | P60/r' |
| 2458353.699 | $18.17 \pm 0.03$ | $26.563 \pm 0.734$ | P60/g' |
| 2458353.7021 | $18.23 \pm 0.02$ | $9.907 \pm 0.183$ | P60/i' |
| 2458352.067 | $18.55 \pm 0.10$ | $62.282 \pm 5.992$ | *Swift*/UVW1 |
| 2458352.074 | $18.48 \pm 0.23$ | $104.091 \pm 22.299$ | *Swift*/UVW2 |
| 2458352.132 | $18.71 \pm 0.09$ | $70.281 \pm 6.024$ | *Swift*/UVM2 |
| 2458352.071 | $18.36 \pm 0.13$ | $40.883 \pm 4.793$ | *Swift*/u |

NOTE. — **Photometry.** This table is available in its entirety in machine-readable format in the online journal. A portion is shown here for guidance regarding its form and content.

*Swift* observations of the SN 2018 fif field started on 2018 August 21 and 11 observations were obtained with a cadence of $\sim 1$ day.

Observations from the 1.2m Schmidt telescope at Palomar Observatory (P48) were obtained using the ZTF mosaic camera composed of 16 6K×6K CCDs (e.g. Bellm et al. 2015) through SDSS $r$-band and $g$-band filters. Data were obtained with a cadence of 3 to 6 observations per day, to a limiting magnitude of R ≈20.5 mag [AB]. ZTF data were reduced by the ZTF photometric pipeline (Masci et al. 2019) employing the optimal image subtraction algorithm of Zackay et al. (2016).

Observations from the robotic 1.52 m telescope at Palomar (P60; Cenko et al. 2006) were obtained using the rainbow camera arm of the SED Machine spectrograph (Blagorodnova et al. 2018), equipped with a $2048 \times 2048$-pixel CCD camera and $g'$, $r'$, and $i'$ SDSS filters. P60 data were reduced using the FPipe pipeline (Fremling et al. 2016).

### 2.3. *Spectroscopy*

Fifteen optical spectra of SN 2018 fif were obtained using the telescopes and spectrographs listed in Table 3. All the observations were corrected for a galactic extinction of $E_{B-V} = 0.10$ mag, deduced from Schlafly & Finkbeiner (2011) and using Cardelli et al. (1989) extinction curves.

We calibrated our spectroscopic data in the following way. Following standard spectroscopic reduction, all spectra were scalled so that their synthetic photometry matches contemporaneous P48 $r$-band value. All spectra are shown in Figure 3 and are available via WISeREP.

## 3. ANALYSIS

### 3.1. *Epoch of first light*

We fitted the P48 r-band rising flux during the first week with a function of the form

$$f = a(t - t_0)^n\,, \quad (1)$$

where $t_0$ is the time of zero flux. This allowed us to estimate the epoch at which the extrapolated light curve is crossing zero, which is used throughout this paper as the reference time $t_0(MJD) = 58351.1537^{+0.0356}_{-0.0903}$ (2018 Aug 21 at 03:41:19.680 UTC). In section 4.3, we show that the explosion time predicted by the Sapir & Waxman (2017) model for shock-cooling emission is earlier, and discuss this point.

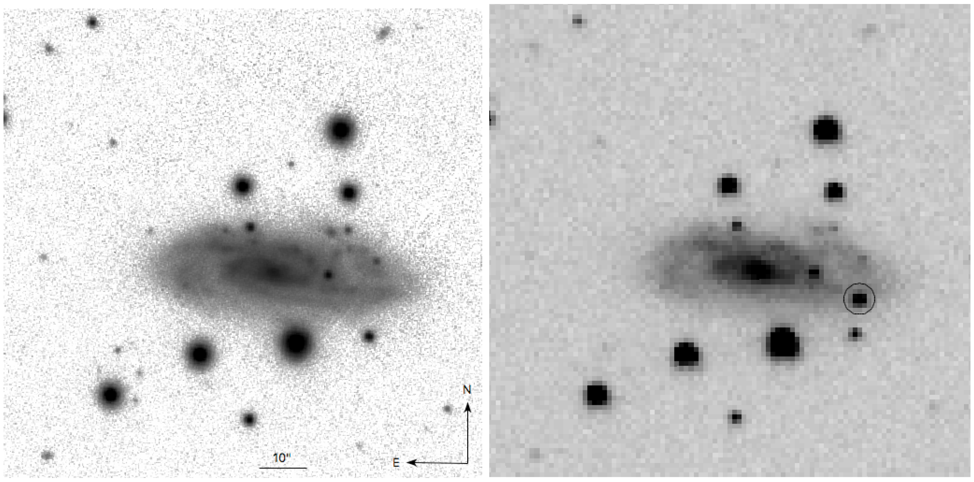


FIG. 1.— Left panel: the PS1 image[a] of UGC 85, the host galaxy of the supernova SN 2018 fif. Right panel: the P48 image of SN 2018 fif close to peak. The circle is centered on the SN position: $\alpha = 2.360644°$ and $\delta = 47.354093°$.

[a]http://ps1images.stsci.edu

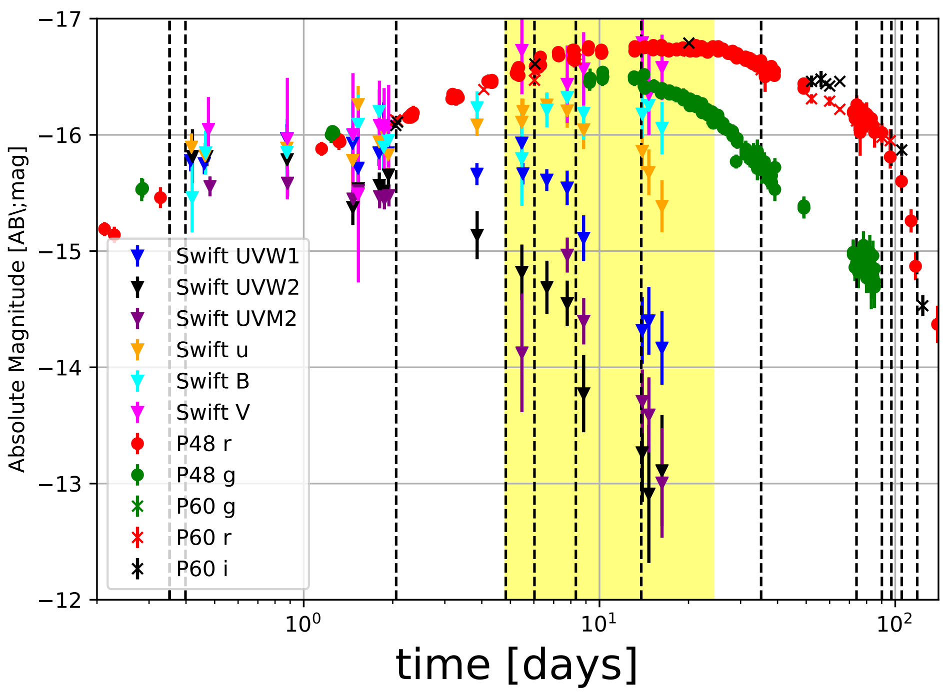


FIG. 2.— The light curve of SN 2018 fif. Time is shown relative to the estimated epoch at which the extrapolated light curve (Equation 1) is crossing zero: $t_0 = 2458351.6537$, as derived in § 3.1. Black dashed lines indicate dates at which spectroscopic data exist. The yellow background indicates the validity domain of the Sapir & Waxman (2017) best fit model:$[4.81, 24.24]$ days.

### 3.2. *Black body temperature and radius*

Taking advantage of the multiple-band photometric coverage, we derived the temperature and radius of the black body that best fits the photometric data at each epoch after interpolating the various data sets to obtain data coverage at coinciding epochs, and deriving the errors at the interpolated points with Monte Carlo Markov chain simulations. This was performed using the `PhotoFit`[3] tool, which is released in the appendix. The interpolated SEDs are shown in Figure 4. The derived best-fit temperatures $T_{BB}$ and radii $r_{BB}$ are shown and compared to those derived for SN 2013 fs in Figure 5.

[3] https://github.com/maayane/PhotoFit

### 3.3. *Bolometric light curve*

Based on the measurement of $r_{BB}$ and $T_{BB}$, we were able to derive the luminosity $L_{BB} = 4\pi R^2\sigma T^4$ of the blackbody fits, shown in Figure 6. It is interesting to note that the bolometric peak occurs early on during the UV-dominated hot shock-cooling phase, well before the apparent peak at visible light.

TABLE 3

| Date | Facility | Reference | Phase |
|---|---|---|---|
| 2018 Aug 21 | P200 + DBSP | [1] | +0.35 days |
| 2018 Aug 21 | P60 + SEDM | [3] | +0.35 days |
| 2018 Aug 21 | Gemini N + GMOS | [2] | +0.40 days |
| 2018 Aug 23 | P60 + SEDM | [3] | +2.05 days |
| 2018 Aug 25 | LT + SPRAT | [4] | +4.82 days |
| 2018 Aug 27 | P60 + SEDM | [3] | +6.03 days |
| 2018 Aug 29 | P60 + SEDM | [3] | +8.32 days |
| 2018 Sep 4 | NOT + ALFOSC | - | +13.85 days |
| 2018 Sep 25 | P60 + SEDM | [3] | +35.20 days |
| 2018 Sep 25 | P60 + SEDM | [3] | +35.20 days |
| 2018 Nov 3 | P60 + SEDM | [3] | +73.96 days |
| 2018 Nov 19 | P60 + SEDM | [3] | +90.11 days |
| 2018 Nov 26 | P60 + SEDM | [3] | +97.04 days |
| 2018 Dec 04 | P60 + SEDM | [3] | +105.17 days |
| 2018 Dec 17 | WHT+ ACAM | [5] | +118.68 days |

NOTE. — Spectroscopic observations of SN 2018 fif. [1]:Oke & Gunn (1982); [2]:Oke et al. (1994); [3]:Blagorodnova et al. (2018); [4]:Steele et al. (2004); [5]:Benn et al. (2008)

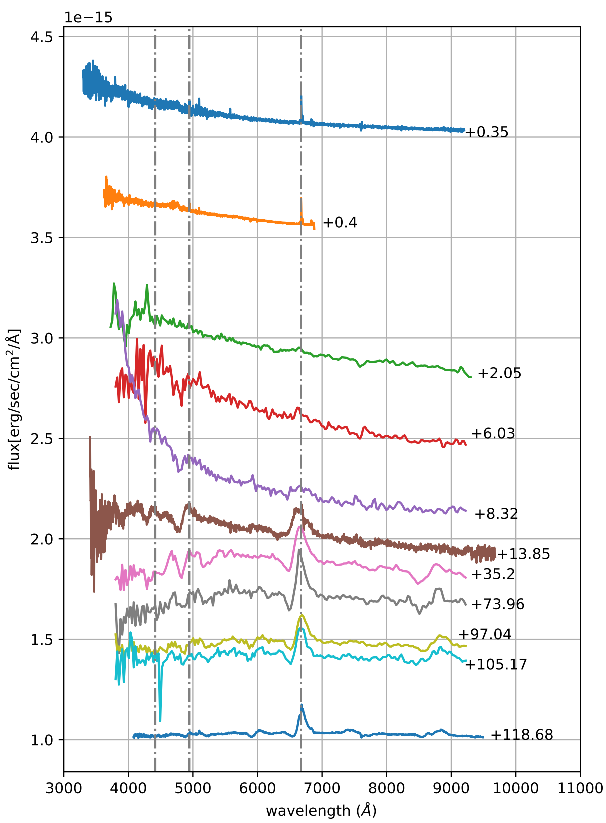


FIG. 3.— The observed spectra of SN 2018 fif. An offset was applied for easier visualization. Dashed lines indicate the redshifted emission lines for the Balmer series up to H$\gamma$. The phase is shown relative to the estimated epoch at which the extrapolated r-band light curve (based on Equation 1) is crossing zero: $t_0$ = 2458351.6537 (2018 August 21), as derived in § 3.1. A color version of this figure is available in the online journal.

### 3.4. *Spectroscopy*

Figure 3 shows the spectroscopic evolution of SN 2018fif over 137 d from its estimated explosion time. The sequence is quite typical for Type II SNe (Gal-Yam 2017), initially showing blue, almost featureless spectra, with low-contrast Balmer lines emerging and becoming pronounced after about a week. The spectrum at phase 13.85 d is typical for the early photospheric phase, with a relatively blue continuum and strong Balmer lines, with H$\alpha$ showing a strong emission component, H$\beta$ having a symmetric P-Cygni profile, and H$\gamma$ appearing only in absorption. The spectra continue to develop during the slowly declining light curve phase over several months, with the continuum emission growing redder and lines becoming stronger. The latest spectra approach the nebular phase and are dominated by a strong emission component of the H$\alpha$ line, emerging emission lines of Ca II (at 7300Å as well as the IR triplet), weaker OI (7774Å and a hint of 6300Å) and Na D.

Focusing on the earliest phase, in Figure 7, we show a comparison of the early spectra of SN 2018fif (P200/DBSP and Gemini-N/GMOS at +8.4 and +8.7 hrs from the estimated explosion time, respectively) with the +21 hr NOT/ALFOSC spectrum of SN 2013 fs (Yaron et al. 2017), which is most similar to our data. We note that earlier spectra of SN 2013fs at similar phase to those of SN 2018fif ($6-10$ h after explosion) are dominated by very strong emission lines of OIV and HeII that are not seen in this case.

In the spectrum of SN 2013 fs, the hydrogen Balmer lines show a broadened base and characteristic electron-scattering wings that are a measure of the electron density in the CSM. The spectra of SN 2018 fif do not show such electron-scattering signatures, even at a much earlier time, and the narrow emission lines seem to arise only from host galaxy emission, with similar profiles to other host lines (such as NII and SII, evident right next to the H$\alpha$ line). A signatures of some CSM interaction may appear in the blue part of the spectrum, in a ledge-shaped emission bump near 4600Å. This shape is similar to that seen in the SN 2013fs spectrum, though the sharp emission spikes (in particular of He II 4686Å) are less well defined. The inset in Fig 7 shows a zoom-in of the elevated region around the He II $\lambda$4686 emission line for both the "SN 2018 fif +8.7 hr" and the "SN 2013 fs +21 hr" spectra. Possible emission lines that may contribute to this elevated emission region include N V $\lambda$4604, N II $\lambda$4631,4643 and C IV $\lambda$4658. Although these identifications are not secure (since they are based on single lines that are only marginally above the noise level), it appears likely that a blend of high-ionization lines is responsible for the elevated emission above the blue continuum.

We conclude from this comparison that SN 2018 fif shows weak evidence in its early spectra for CSM surrounding the progenitor, and that the CSM is likely less dense than in the case of SN 2013 fs, as shown by the lack of strong high-ionization lines in the spectra of SN 2018fif at a similar epoch and the sharp profiles of the Balmer lines that show no evidence for electron scattering wings.

## 4. SHOCK COOLING AND PROGENITOR MODEL

### 4.1. *The model*

In order to model the multiple-bands emission from SN 2018 fif, we used the model by Sapir & Waxman (2017), an extension of the model derived in Rabinak & Waxman (2011). In the following, we use the abbreviations "SW17" and "RW11" to refer to the models, as opposed to the papers in which they were published.

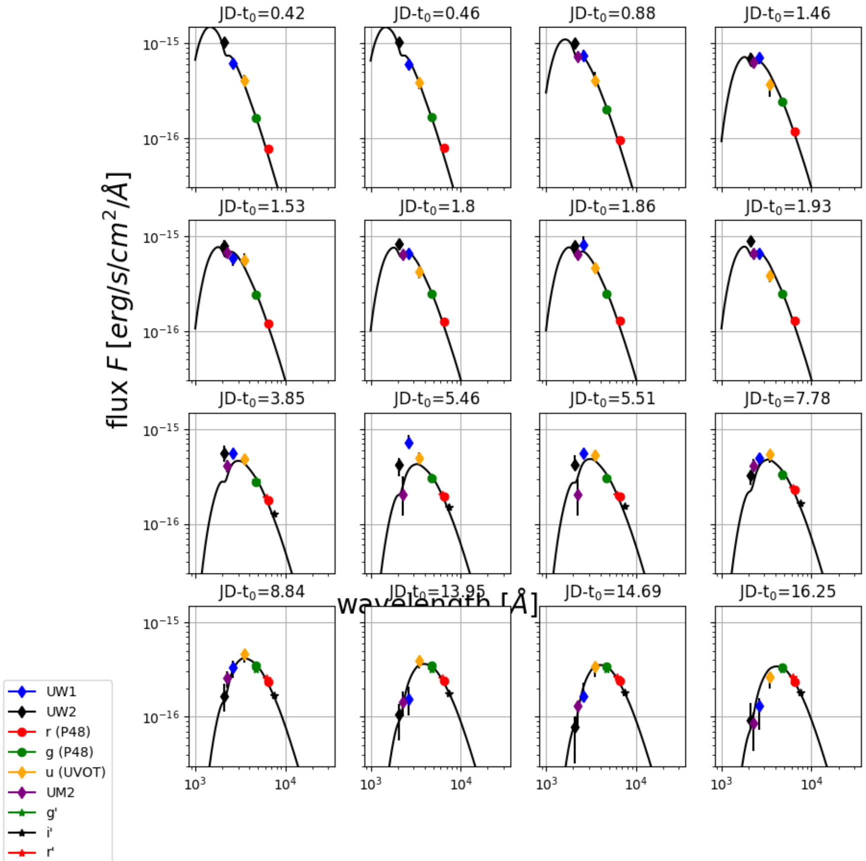


FIG. 4.— Black body fits to Swift/UVOT and optical photometry for 2018fif. Using the `PhotoFit` tool[a], photometric points were interpolated to a common epoch (UVOT epochs), and the errors at the interpolated points were computed with Monte Carlo Markov chain simulations.
[a]https://github.com/maayane/PhotoFit

We summarize below the main conclusions of these two models. Both hold for temperatures $> 0.7\,\mathrm{eV}$, the limit above which Hydrogen is fully ionized, recombination effects can be neglected and the approximation of constant opacity holds.

#### 4.1.1. *The Rabinak & Waxman (2011) model*

Rabinak & Waxman (2011) explored the domain of times when the the emission originates from a thin shell of mass i.e. the radius of the photosphere is close to the radius of the stellar surface. The post-breakout time-evolution of the photospheric temperature and bolometric luminosity, is given by (see also Equation (4) of Sapir & Waxman 2017):

$$T_{\rm ph,RW} = 1.61[1.69]\left(\frac{v_{s*,8.5}^2 t_{\rm d}^2}{f_\rho M_0 \kappa_{0.34}}\right)^{\epsilon_1} \frac{R_{13}^{1/4}}{\kappa_{0.34}^{1/4}} t_{\rm d}^{-1/2}\,{\rm eV}\,, \quad (2)$$

$$L_{\rm RW} = 2.0[2.1]\times 10^{42}\left(\frac{v_{s*,8.5} t_{\rm d}^2}{f_\rho M_0 \kappa_{0.34}}\right)^{\epsilon_2} \frac{v_{s*,8.5}^2 R_{13}}{\kappa_{0.34}}\,{\rm erg/s}\,, \quad (3)$$

where $\kappa = 0.34\kappa_{0.34}{\rm cm}^2\,{\rm g}^{-1}1$, $v_{s*} = 10^{8.5}\,v_{s*,8.5}$, $M = M_0\,M_\odot$, $R = 10^{13}\,R_{13}{\rm cm}$, $\epsilon_1 = 0.027[0.0.016]$ and $\epsilon_2 = 0.086[0.175]$ for convective[radiative] envelopes. $M$ is the mass of the ejecta, $f_\rho$ is a numerical factor of order unity describing the inner structure of the envelope, $t_{\rm d}$ is the time from explosion in days, and $v_{s*}$ is a measure of the shock velocity $v_{\rm sh}$: in regions close to the stellar surface, at radii such as $\delta \equiv (R-r)/R \ll 1$, $v_{\rm sh}$ is linked to $v_{s*}$ through (Gandel'Man & Frank-Kamenetskii 1956; Sakurai 1960)

$$v_{\rm sh} = v_{s*}\delta^{-\beta n}\,, \quad (4)$$

with $\beta = 0.191[0.186]$, and $v_{s*}$ only depends on E, M (the ejecta energy and mass) and $f_\rho$ (Matzner & McKee 1999):

$$v_{s*} \approx 1.05 f_\rho^{-\beta}\sqrt{E/M}\,, \quad (5)$$

The RW11 model holds during a limited temporal range. The upper limit on this range,

$$t < 3 f_\rho^{-0.1}\frac{\sqrt{\kappa_{0.34} M_0}}{v_{s*,8.5}}\,{\rm days} \quad (6)$$

follows from the requirement that the emitting shell carry

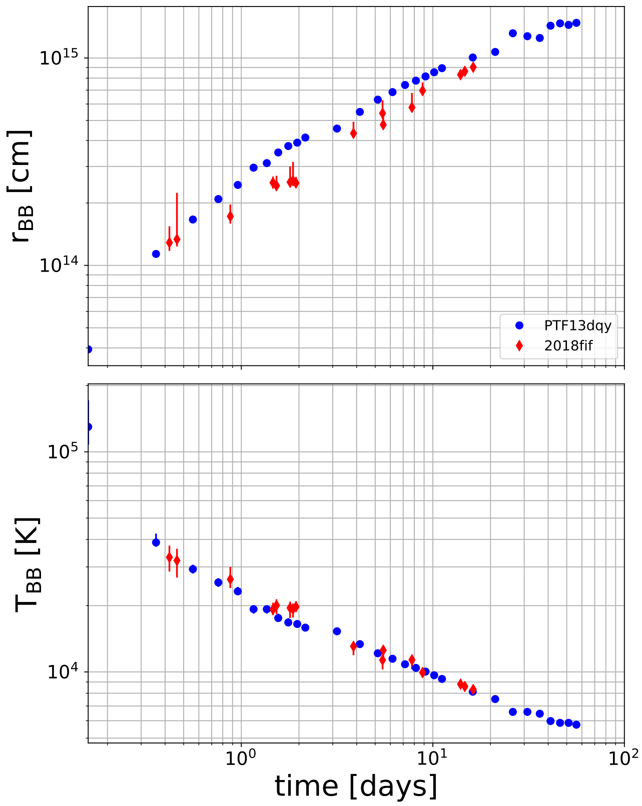


FIG. 5.— The evolution in time of: (1) the radius (top panel) and (2) the temperature (lower panel) of a blackbody with the same radiation as SN 2018 fif (red) and SN 2013 fs (blue), for comparison. For SN 2018 fif, the points were obtained by fitting a black body spectrum to the observed photometry, after interpolating the various data sets to obtain data coverage at coinciding epochs. The errors were obtained with Monte Carlo Markov chain simulations. The SN 2013 fs results were taken from Yaron et al. (2017).

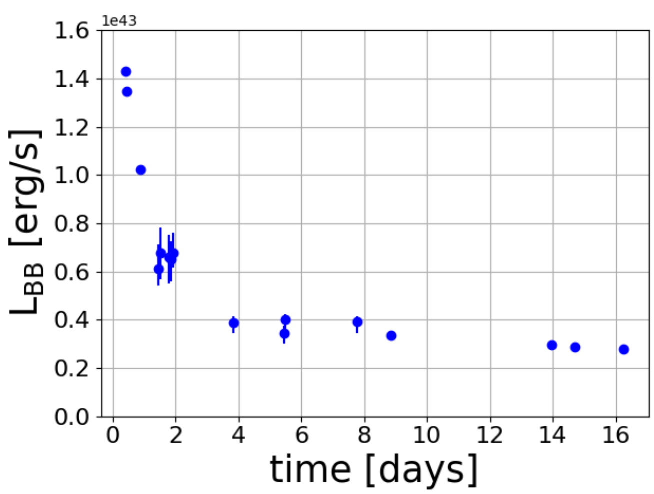


FIG. 6.— The evolution in time of the bolometric luminosity of a blackbody with the same radiation as SN 2018 fif.

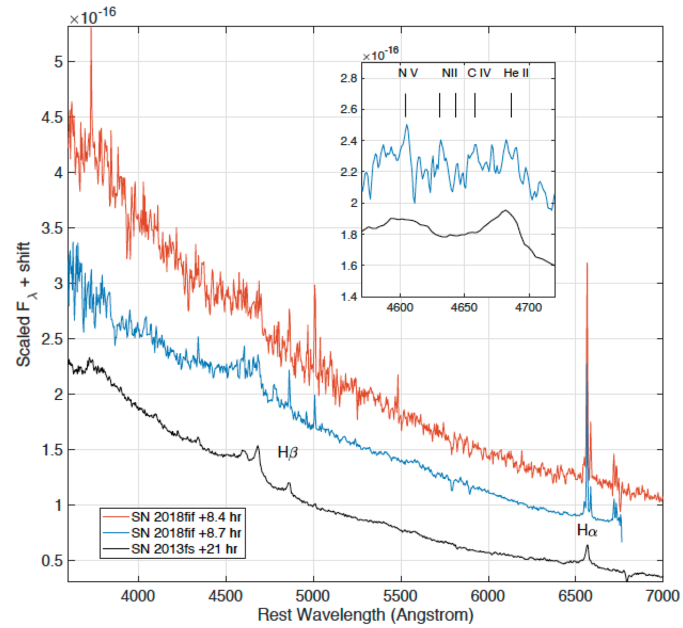


FIG. 7.— Comparison of early spectra of SN 2018 fif (at 8.7 hr) and SN 2013 fs (at 21 hr; from Yaron et al. 2017). SN 2018 fif shows sharp, narrow Balmer lines lacking a broad electron-scattering base. A broad ledge around 4600Åindicates a likely blend of weak high-ionization lines, suggestion some CSM emission does exist in this event, though less than in SN 2013 fs, see text.

a small fraction of the ejecta mass. The lower limit

$$t > 0.2\frac{R_{13}}{v_{s*8.5}} max\left[0.5, \frac{R_{13}^{0.4}}{(f_\rho \kappa_{0.34} M_0)^{0}.2 v_{s*8.5}^{0.7}}\right] \quad (7)$$

comes from two different requirements: (1) The photosphere must have penetrated beyond the thickness at which the initial breakout happens (see equation (16) of RW11) and (2) Expansion must be significant enough so that the ejecta are no longer planar and have become spherical (Waxman & Katz 2017); this last requirement was added Sapir & Waxman (2017).

#### 4.1.2. *The Sapir & Waxman (2017) model*

Sapir & Waxman (2017) extended the RW11 description to later times, when the photosphere has penetrated more deeply into the envelope, but is still close enough to the surface so that the emission is still weakly dependent on the inner structure of the envelope. As radiation originates from inner regions, the self-similar description of the shock-wave (Gandel'Man & Frank-Kamenetskii 1956; Sakurai 1960), one of the key ingredients of the RW11 model, does not hold anymore. This results in a suppression of the bolometric luminosity that can be approximated by (equation (14) of Sapir & Waxman 2017):

$$L/L_{\rm RW} = A \exp\left[-\left(\frac{at}{t_{\rm tr}}\right)^{\alpha}\right], \quad (8)$$

where $A = 0.94[0.79]$, $a = 1.67[4.57]$ and $\alpha = 0.8[0.73]$ for convective[radiative] envelopes. The thin shell requirement (Equation 6) is relaxed, and the new upper limit of the validity time range is dictated by the requirement of constant opacity:

$$t < min(t_{\rm tr}/a, t_{\rm T<0.7})\,, \qquad (9)$$

where $t_{\rm tr}$ is the time beyond which the envelope becomes transparent, and $t_{\rm T<0.7}$ is the time when T drops below 0.7 eV and recombination leads to a decrease of the opacity.

The observed flux, for a SN at distance $D$ and redshift $z$ is given by

$$\begin{aligned} f_\lambda(\lambda,t) &= \frac{L(t)}{4\pi D^2 \sigma T_{col}^4}(z+1)^4 B_\lambda(\lambda, T_{\rm col,z}) \\ &= \left(\frac{R(t)}{D}\right)^2 (z+1)^4 B_\lambda(\lambda, T_{\rm col,z})\,, \end{aligned} \qquad (10)$$

where $T_{\rm col}/T_{\rm ph,RW} = 1.1[1.0] \pm 0.05$ for convective[radiative] envelopes, $L$ is the bolometric luminosity given in equation 8 and $T_{\rm col,z} = T_{\rm col}/(z+1)$ is the temperature of a blackbody with intrinsic temperature $T_{\rm col}$, observed at redshift $z$.

### 4.2. *The* SOPRANO *algorithm*

The main difficulty in implementing the SW17 model is that the temporal validity domain of the model depends on the parameters of the model themselves. In other worlds, different combinations of the model's parameters correspond to different data to fit (Rubin & Gal-Yam 2017). One way to cope with this difficulty is to fit the data on a chosen range of times, and to retrospectively assess whether the solution is valid in this temporal window. This approach, which was taken e.g. by Valenti et al. (2014); Bose et al. (2015); Rubin et al. (2016) and Hosseinzadeh et al. (2019), is not fully satisfactory for several reasons: (1) it may limit the explored area in the parameters space, since this area is pre-defined by the choice of the data temporal window and (2) it makes it impossible to make a fair comparison between models, as the goodness of a model should be judged on nothing more or less than its specific validity range: a good model fits the data on its *entire* validity range and *only* on its validity range. It is clear that the best-fit model (and hence deduced progenitor parameters) may depend on the arbitrary choice of pre-defined data modeled, which is not a good result.

Here, we adopt a self-consistent approach and build an algorithm to find models that fit well the data included in their entire range of validity. In this sense, our approach is similar to the one adopted by Rubin & Gal-Yam (2017). The `SOPRANO` algorithm (ShOck cooling modeling with saPiR & wAxman model by gANot & sOumagnac, Ganot et al. in preparation) is available in two versions: `SOPRANO-grid`, written in `matlab` and `SOPRANO-mcmc`, written in `python`. Both will shortly be released to the community (Ganot et al., in preparation). The steps of `SOPRANO-grid` are as follows:

- we build a 6-dimensional grid of parameters $\{\rm R, v_{s*,8.5}, t_0, M, f_\rho, E_{B-V}\}$: a given point in the grid (indexed e.g. $j$, for clarity) corresponds to a model $\mathcal{M}_j$;

- we calculate, for each point in the grid, the time-validity domain, and deduce from it the set of $N_j$ data points $\{x_i, y_i\}_{i\in[1,N_j]}$ (with uncertainties $\sigma_{y_i}$ on the $y_i$ values) to be taken into account in the fit of model $\mathcal{M}_j$ to the data;

- we calculate a probability for each point in the grid, using
$$P_j = PDF(\chi^2_j, \nu_j)\,, \qquad (11)$$
where $\nu_j$ is the number of degrees of freedom (this number varies between models, as the validity domain - and hence the number of points included in the data - varies), $\chi^2_j$ is the chi-square statistic of the fit, for the model $\mathcal{M}_j$
$$\chi^2_j = \sum_{i=1}^{N_j} \frac{(y_i - \mathcal{M}_j(x_i))^2}{\sigma^2_{yi}} \qquad (12)$$
and $PDF$ is the chi-squared probability distribution function.

The output of this procedure is a grid of probabilities, which we can compare to each other to find the most probable model. In order to have a sensitive radius measurement (the progenitor radius is measured through the explosion temperature temporal change, and the largest change occurs at early times, when the UV channels peak), we required at least three UV points to be within the time validity domain of a model. The models labeled as invalid through this procedure have non-physical parameters.

The second version of the `SOPRANO` algorithm, `SOPRANO-mcmc`, uses the model probability defined in equation 11 as the input of a MarKov Chain Monte Carlo simulation. No specific requirement on the amount of UV points within the time validity domain is applied.

In both cases, we apply the following flat priors for the six parameters of our model: $R \in [200, 2000]$, $v_{s*,8.5} \in [0.3, 1.5]$, $M \in [1, 25]$, $f_\rho \in [\sqrt{1/3}, \sqrt{10}]$ (Sapir & Waxman 2017), $t_{\rm exp} \in [2458348.5, t_0]$, $E_{\rm B-V} \in [0.1, 0.25]$. The prior on the radius $R$ was chosen to reflect current measurements (Davies et al. 2018; see Figure 10). The prior on $f_\rho \in [\sqrt{1/3}, \sqrt{10}]$ corresponds to the range used in the model by Sapir & Waxman (2017). The choice of priors for $t_{\rm exp}$, $v_{s*,8.5}$ and $E_{\rm B-V} \in [0.1, 0.25]$ is the result of an iterative process (coarse to fine grid) aiming at finding the relevant location in the parameters space while limiting the memory use and running-time.

Note that our approach is similar to the one by Rubin & Gal-Yam (2017), in the sense that it is self-consistent and takes care of the time-validity issue. However, the strategy adopted to compare and discriminate between models (equation 11) is different.

### 4.3. *Results*

In figure 9, we show the two dimensional projections of the pdf distributions obtained by fitting our model to the data, obtained with `SOPARANO-mcmc`. In order to compute the best-fit parameters, we ran the `matlab` optimizing algorithm `fminsearch`, that minimizes the six-parameter function $1-pdf$, setting the initial conditions to the maximum of the grid computed by `SOPARANO-grid` (another possibility is to set the initial

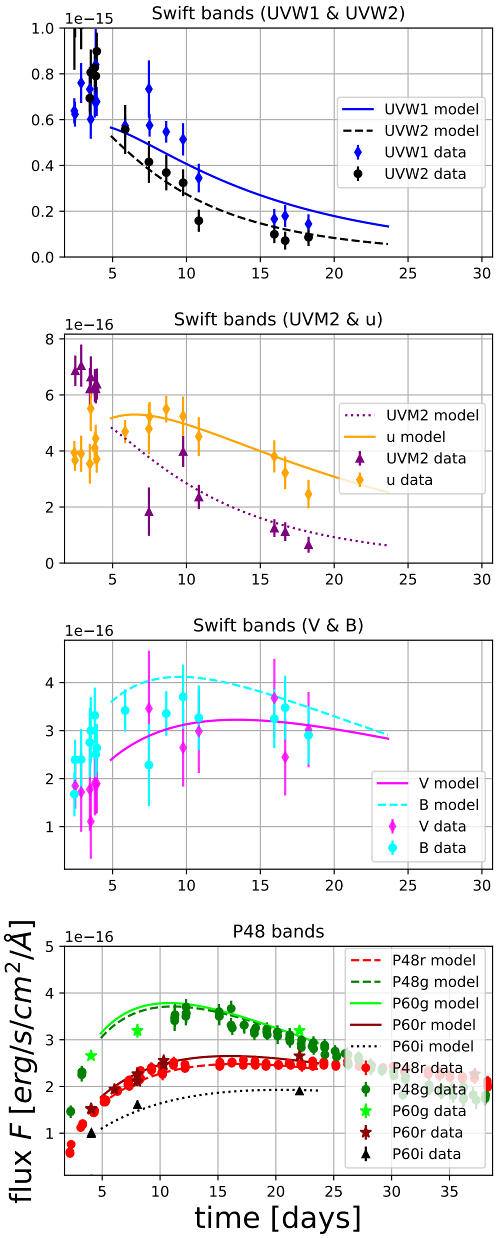


FIG. 8.— Best fit Sapir & Waxman model ($\chi^2/dof = 1.13$) superimposed with the photometric data of SN 2018 fif.

conditions to the maximum of the MCMC chain computed by `SOPARANO-mcmc`). Note that when the probability function is not purely Gaussian (e.g. if it is double-peaked, which is the case here) or is asymmetric, the maximum probability does not fall necessarily close to the median of the marginalized distributions. In particular, it can fall outside of the symmetric interval containing 68% of the probability, which is often reported as the $1\sigma$-confidence range, and does not reflect any asymmetry of the distribution. Here, we report instead the tightest intervals containing 68% of the probability and including our best-fit values.

A full tabulation of the best-fit parameters, as well as the median and 68.2% confidence range for each parameter computed with `SOPARANO-mcmc` is shown in table 4. We checked that they are consistent with the confidence intervals computed with `SOPARANO-grid`. The best fit parameters correspond to $\chi^2/dof = 1.13$ and are : $R = 1204^{+121.52}_{-176.31}\,R_\odot$, $M_{\rm ej} = 10.5^{+6.4}_{-0.0}\,M_\odot$, $t_{\rm exp} = 2458349.54^{+0.84}_{-0.25}$ JD, $E_{\rm B-V} = 0.216^{+0.0}_{-0.047}$, $f_\rho = 2.19^{+0.29}_{-0.97}$ and $v_{\rm s*,8.5} = 0.620^{+0.076}_{-0.062}$. The temporal validity window of this model is $[4.81, 24.24]$ days. In Figure 8, we show a comparison of the data and the best-fit model. We comment on the best-fit results below:

TABLE 4

| Parameter name | Best fit | Median of posterior distr. | 68.2% confidence range |
|---|---|---|---|
| $R$ | 1204 | 1135.83 | $[1027.69, 1325.52]$ |
| $v_{\rm s*,8.5}$ | 0.62 | 0.62 | $[0.56, 0.7]$ |
| $M$ | 10.5 | 14.5 | $[10.5, 16.9]$ |
| $t_{\rm exp}$ | 2458349.54 | 2458349.76 | $[2458349.29, 2458350.38]$ |
| $E_{\rm B-V}$ | 0.216 | 0.189 | $[0.169, 0.216]$ |
| $f_\rho$ | 2.19 | 1.96 | $[1.22, 2.48]$ |
| $\chi^2/dof$ | 1.13 | 8.632 | – |

NOTE. — Results of the model fitting. The table shows the best-fit parameters, the median values of the MCMC chains, and 68.2% confidence range for each parameter, computed using the marginalised posterior distributions

- In figure 10, we show red supergiant (RSG) radii and luminosities derived from the temperatures and luminosities measured by Davies et al. (2018) for RSGs in the small and large Magellanic Clouds (SMC and LMC). The best-fit value of the radius we find for the SN 2018 fif progenitor star, $R = 1204^{121.52}_{176.31}\,R_\odot$, is within but at the high end of the range of radii measured for RSGs.

- The value of $t_{\rm exp}$, the epoch of the explosion predicted by our model, is earlier than $t_0 2458351.6537^{+0.0356}_{-0.0903}$ JD, the estimated epoch at which the extrapolated r-band light curve is crossing zero. This is not surprising: $t_0$ is a measure of the epoch of first-light in *the r-band* and hot young SNe are predicted to emit light in the UV before they significantly emit optical light: there is no reason for $t_0$ and $t_{\rm exp}$ to be identical. Moreover, this discrepancy between $t_{\rm exp}$ and $t_0$ is observed in other cases: in the *GALEX*-PTF sample, to be published by Ganot et al. (in preparation), it can reach several days, like here.

- The relatively high range of values of $f_\rho$ corresponds to a high ratio of $M_{\rm env}/M_{\rm c}$, where $M_{\rm env}$ is the mass of the envelope (see Figure 5 of Sapir & Waxman 2017).

- The best-fit value of the extinction $E_{\rm B-V} = 0.216^{0.0}_{0.047}$ is high: note that it is the sum of the galactic extinction $E_{\rm B-V} = 0.10$ (deduced from Schlafly & Finkbeiner 2011 and using Cardelli et al. 1989 extinction curves) and all other sources of extinction along the line of sight, including the extinction from the SN host galaxy. The galactic extinction has a relatively high contribution to the derived value of $E_{\rm B-V}$.

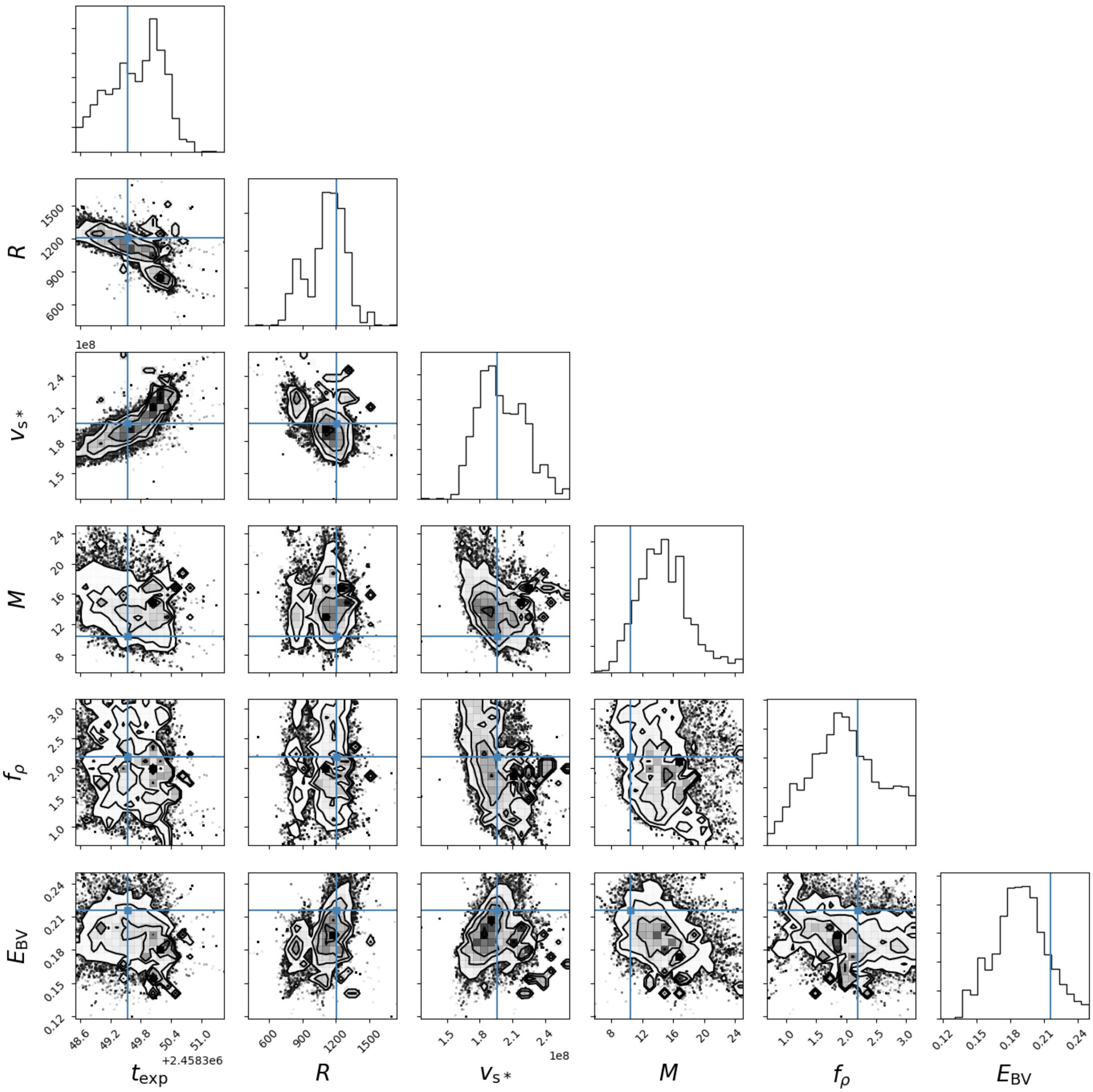


FIG. 9.— All the one and two dimensional projections of the posterior probability distributions of the parameters $R$, $v_{\mathrm{s}*,8.5}$, $M$, $f_\rho$, $t_{\mathrm{exp}}$, $E_{\mathrm{B-V}}$. This quickly demonstrates all of the covariances between parameters. The contours correspond to the $1\sigma$, $2\sigma$ and $3\sigma$ symmetric percentiles. The blue line corresponds to the maximum probability value calculated with the **matlab** optimizing algorithm **fminsearch**, setting the initial conditions to the maximum of the grid computed by `SOPARANO-grid`.

- In order to verify whether our best-fit value for $v_{\mathrm{s}*,8.5}$ is consistent with the observations, we make an order of magnitudes estimate of $\mathrm{v}_{sh}$ using equations 4 and 5 and equation (11) from Rabinak & Waxman (2011), which provides an expression of the depth $\delta$ as a function of our model parameters. We obtain that the predicted value of the velocity of the shock wave is $v_{sh} \approx 9800\,\mathrm{km/s}$. We use the P-Cygni profile of the H line in the spectrum of SN 2018 fif at $t = +13.85\,\mathrm{days}$ to estimate the observed velocity $v \approx 10\,000\,\mathrm{km/s}$ and find that it is consistent with the model prediction.

## 5. CONCLUSIONS

We presented the observations of the SN 2018 fif by ZTF and *Swift*. The analysis of the early spectroscopic observations of SN 2018 fif reveals that its progenitor was surrounded by relatively small amounts of circumstellar material compared to a handful of previous cases. This specificity, as well as the high cadence multiple-bands coverage, make it a good candidate to test shock-cooling models.

We employ the `SOPRANO` code, an implementation

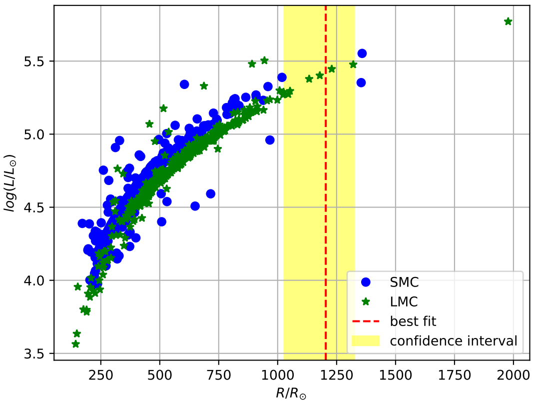


FIG. 10.— Radii and luminosities of the stars in the small and large Magellanic Clouds. They were derived from the effective temperatures and luminosities published by Davies et al. (2018) (Figure 5).

of the model by Sapir & Waxman (2017), which will soon be available to the community in its two versions, `SOPRANO-grid` (`matlab`) and `SOPRANO-mcmc` (`python`). The `SOPRANO` algorithm has the advantage of being self-consistent, by including a careful account for the model validity time domain.

We find that the progenitor of SN 2018 fif was a large red super-giant, with a radius of $R/R_{\odot} = 1204^{121.52}_{176.31}$ and an ejected mass of $M/M_{\odot} = 10.5^{6.4}_{0.0}$. Our model also gives information on the explosion epoch, the progenitor inner structure, the shock velocity and the extinction. The large radius differs from previously modeled objects, and the difference could be either intrinsic (differing progenitors) or due to the relatively small amount of CSM around SN 2018 fif, perhaps making it a cleaner candidate for applying shock cooling analytical models.

As new wide-field transient surveys such as the Zwicky Transient Facility (e.g., Bellm et al. 2019; Graham et al. 2019) are deployed, many more SNe will be observed early, and quickly followed up with early spectroscopic observation and multiple-band photometric observations.

The ULTRASAT UV satellite mission (Sagiv et al. 2014) will also collect early UV light curves of hundreds of core-collapse supernovae. The methodology proposed in this paper offers a framework to analyze these objects, in order to constrain the properties of their massive progenitors and pave the way to a comprehensive understanding of the final evolution and explosive death of massive stars.

We dedicate this paper to the memory of Rona Ramon.

M.T.S. thanks X for useful discussions. M.T.S. acknowledges support by a grant from IMOS/ISA, the Ilan Ramon fellowship from the Israel Ministry of Science and Technology and the Benoziyo center for Astrophysics at the Weizmann Institute of Science.

E.O.O is grateful for the support by grants from the Israel Science Foundation, Minerva, Israeli Ministry of Science, the US-Israel Binational Science Foundation, the Weizmann Institute and the I-CORE Program of the Planning and Budgeting Committee and the Israel Science Foundation.

A.G.-Y. is supported by the EU via ERC grant No. 725161, the Quantum Universe I-Core program, the ISF, the BSF Transformative program, IMOS via ISA and by a Kimmel award.

The data presented here are based - in part - on observations obtained with the Samuel Oschin Telescope 48-inch and the 60-inch Telescope at the Palomar Observatory as part of the Zwicky Transient Facility project. ZTF is supported by the National Science Foundation under Grant No. AST-1440341 and a collaboration including Caltech, IPAC, the Weizmann Institute for Science, the Oskar Klein Center at Stockholm University, the University of Maryland, the University of Washington, Deutsches Elektronen-Synchrotron and Humboldt University, Los Alamos National Laboratories, the TANGO Consortium of Taiwan, the University of Wisconsin at Milwaukee, and Lawrence Berkeley National Laboratories. Operations are conducted by COO, IPAC, and UW.

SED Machine is based upon work supported by the National Science Foundation under Grant No. 1106171

The data presented here were obtained - in part - with ALFOSC, which is provided by the Instituto de Astrofisica de Andalucia (IAA) under a joint agreement with the University of Copenhagen and NOTSA.The Liverpool Telescope, located on the island of La Palma in the Spanish Observatorio del Roque de los Muchachos of the Instituto de Astrofisica de Canarias, is operated by Liverpool John Moores University with financial support from the UK Science and Technology Facilities Council.The ACAM spectroscopy was obtained as part of OPT/2018B/011.

# APPENDIX

## RELEASE OF THE `PHOTOFIT` CODE

## REFERENCES

Arcavi, I., Hosseinzadeh, G., Brown, P. J., et al. 2017, ApJ, 837, L2

Bellm, E. C., Kulkarni, S. R., & ZTF Collaboration. 2015, in American Astronomical Society Meeting Abstracts, Vol. 225, American Astronomical Society Meeting Abstracts #225, 328.04

Bellm, E. C., Kulkarni, S. R., Graham, M. J., et al. 2019, Publications of the Astronomical Society of the Pacific, 131, 018002

Benn, C., Dee, K., & Agócs, T. 2008, in Proc. SPIE, Vol. 7014, Ground-based and Airborne Instrumentation for Astronomy II, 70146X

Blagorodnova, N., Neill, J. D., Walters, R., et al. 2018, PASP, 130, 035003

Bose, S., Valenti, S., Misra, K., et al. 2015, MNRAS, 450, 2373

Cardelli, J. A., Clayton, G. C., & Mathis, J. S. 1989, ApJ, 345, 245

Cenko, S. B., Fox, D. B., Moon, D.-S., et al. 2006, PASP, 118, 1396

Davies, B., Crowther, P. A., & Beasor, E. R. 2018, MNRAS, 478, 3138

Falco, E. E., Kurtz, M. J., Geller, M. J., et al. 1999, Publications of the Astronomical Society of the Pacific, 111, 438

Fremling, C. 2018, Transient Name Server Discovery Report, 1231

Fremling, C., Sollerman, J., Taddia, F., et al. 2016, A&A, 593, A68

Gal-Yam, A. 2017, Observational and Physical Classification of Supernovae, ed. A. W. Alsabti & P. Murdin, 195

Gal-Yam, A. 2019, in American Astronomical Society Meeting Abstracts, Vol. 233, American Astronomical Society Meeting Abstracts #233, 131.06

Gal-Yam, A., Kasliwal, M. M., Arcavi, I., et al. 2011, ApJ, 736, 159

Gal-Yam, A., Arcavi, I., Ofek, E. O., et al. 2014, Nature, 509, 471

Gall, E. E. E., Polshaw, J., Kotak, R., et al. 2015, A&A, 582, A3

Gandel'Man, G. M., & Frank-Kamenetskii, D. A. 1956, Soviet Physics Doklady, 1, 223

González-Gaitán, S., Tominaga, N., Molina, J., et al. 2015, MNRAS, 451, 2212

Graham, M. J., Kulkarni, S. R., Bellm, E. C., et al. 2019, arXiv e-prints, arXiv:1902.01945

Hosseinzadeh, G., McCully, C., Zabludoff, A. I., et al. 2019, ApJ, 871, L9

Hosseinzadeh, G., Valenti, S., McCully, C., et al. 2018, ApJ, 861, 63

Kasliwal, M. M., Cannella, C., Bagdasaryan, A., et al. 2019, PASP, 131, 038003

Khazov, D., Yaron, O., Gal-Yam, A., et al. 2016, ApJ, 818, 3

Levesque, E. M. 2017, Astrophysics of Red Supergiants, doi:10.1088/978-0-7503-1329-2

Masci, F. J., Laher, R. R., Rusholme, B., et al. 2019, PASP, 131, 018003

Matzner, C. D., & McKee, C. F. 1999, ApJ, 510, 379

Morozova, V., Piro, A. L., Renzo, M., & Ott, C. D. 2016, ApJ, 829, 109

Nugent, P. E., Sullivan, M., Cenko, S. B., et al. 2011, Nature, 480, 344

Oke, J. B., & Gunn, J. E. 1982, PASP, 94, 586

Oke, J. B., Cohen, J. G., Carr, M., et al. 1994, in Proc. SPIE, Vol. 2198, Instrumentation in Astronomy VIII, ed. D. L. Crawford & E. R. Craine, 178–184

Patterson, M. T., Bellm, E. C., Rusholme, B., et al. 2019, PASP, 131, 018001

Rabinak, I., & Waxman, E. 2011, ApJ, 728, 63

Rubin, A., & Gal-Yam, A. 2017, ApJ, 848, 8

Rubin, A., Gal-Yam, A., De Cia, A., et al. 2016, ApJ, 820, 33

Sagiv, I., Gal-Yam, A., Ofek, E. O., et al. 2014, AJ, 147, 79

Sakurai, A. 1960, Communications on Pure and Applied Mathematics, 13, doi:10.1002/cpa.3160130303

Sapir, N., & Waxman, E. 2017, ApJ, 838, 130

Schlafly, E. F., & Finkbeiner, D. P. 2011, ApJ, 737, 103

Smartt, S. J. 2015, , 32, e016

Steele, I. A., Smith, R. J., Rees, P. C., et al. 2004, in Proc. SPIE, Vol. 5489, Ground-based Telescopes, ed. J. M. Oschmann, Jr., 679–692

Tartaglia, L., Fraser, M., Sand, D. J., et al. 2017, ApJ, 836, L12

Valenti, S., Sand, D., Pastorello, A., et al. 2014, MNRAS, 438, L101

Waxman, E., & Katz, B. 2017, Shock Breakout Theory, 967

Yaron, O., & Gal-Yam, A. 2012, PASP, 124, 668

Yaron, O., Perley, D. A., Gal-Yam, A., et al. 2017, Nature Physics, 13, 510

Zackay, B., Ofek, E. O., & Gal-Yam, A. 2016, ApJ, 830, 27